Solution-doped donor-acceptor copolymers based on diketopyrrolopyrrole and 3, 3'-bis (2-(2-(2-methoxyethoxy) ethoxy) ethoxy)-2, 2'-bithiophene exhibiting outstanding thermoelectric power factors with p-dopants

*Tushita Mukhopadhyaya, Justine Wagner, Taein D. Lee, Connor Ganley, Swati Tanwar, Piyush Raj, Lulin Li, Yunjia Song, Sophia J. Melvin, Yuyang Ji, Paulette Clancy, Ishan Barman, Susanna Thon, Rebekka S. Klausen and Howard E. Katz**

T. Mukhopadhyaya, T. D. Lee, Y. Song, H. E. Katz
Johns Hopkins University, Department of Materials Science and Engineering, 3400 N Charles Street, Baltimore, MD 20218
E-mail: hekatz@jhu.edu

C. Ganley, P. Clancy
Johns Hopkins University, Department of Chemical and Biomolecular Engineering, 3400 N Charles Street, Baltimore, MD 21218

S. Tanwar, P. Raj, I. Barman
Johns Hopkins University, Department of Mechanical Engineering, 3400 N Charles Street, Baltimore, MD 21218

Sophia J. Melvin, Yuyang Ji, Rebekka S. Klausen
Johns Hopkins University, 3400 N Charles Street, Department of Chemistry, 3400 N Charles Street, Baltimore, MD 21218

L. Li, S. Thon
Johns Hopkins University, 3400 N Charles Street, Department of Electrical and Computer Engineering, 3400 N Charles Street, Baltimore, MD 21218

Keywords: diketopyrrolopyrrole, conducting polymer, dopant, thermoelectric, power factor

Abstract

Design of polymeric semiconductors exhibiting high electrical conductivity (σ) and thermoelectric power factor (PF) will be vital for flexible large-area electronics. In this work, we investigated four polymers based on diketopyrrolopyrrole (DPP), 2,3-dihydrothieno[3,4-b][1,4]dioxine (EDOT), thieno[3,2-b]thiophene (TT) and 3, 3'-bis (2-(2-(2-methoxyethoxy) ethoxy) ethoxy)-2, 2'-bithiophene (MEET) as side-chains, with the MEET polymers newly synthesized for this study. These polymers were systematically doped with F_4TCNQ, CF_3SO_3H and the synthesized dopant $Cp(CN)_3$-$(COOMe)_3$, differing in geometry and electron affinity. The DPP-EDOT based polymer containing MEET as side-chains exhibited the highest σ ~700 S cm^{-1} in this series with the acidic dopant (CF_3SO_3H). This polymer also showed the lowest oxidation potential by cyclic voltammetry (CV), the strongest intermolecular interactions evidenced by differential scanning calorimetry (DSC) and had the most oxygen-based functionality for possible hydrogen bonding and ionic screening. Other polymers exhibited high σ ~300-500 S cm^{-1} and PF up to 300 μW m^{-1} K^{-2}. The mechanism of conductivity is predominantly electronic, as validated by time-dependent conductance studies and transient thermo voltage monitoring over time, including for those doped with the acid. These materials maintained significant thermal stability and air stability over ~6 weeks. Density functional theory calculations revealed molecular geometries and informed about frontier energy levels. Raman spectroscopy, in conjunction with scanning electron microscopy (SEM-EDS) and x-ray diffraction, provided insight into the solid-state microstructure and degree of phase separation of the doped polymer films. Infrared (IR) spectroscopy enabled us to further quantify the degree of charge transfer from polymer to dopant.

1. Introduction

Doped polymer semiconductors have gained increasing attention for large-area and flexible thermoelectric (TE) devices.[1] Semiconductor TE performance is characterized by the figure of merit (ZT), $ZT = S^2\sigma T/\kappa$, where σ, S, κ, and T are respectively the electrical conductivity (σ), Seebeck coefficient, thermal conductivity and absolute temperature, and $S^2\sigma$ is the thermoelectric power factor (PF).[2] Conjugated polymers typically exhibit thermal conductivities of 0.1-2 W m^{-1} K^{-1}.[3] To achieve high ZT values, high σ is a prerequisite, which is driven by high charge carrier mobility and efficiency of the mobile charge-generation process. S is inversely correlated to σ and is proportional to the difference between Fermi level (E_F) and transport level (E_T) for disordered polymer systems.[4] Doping efficiency requires the polymer

to possess a high HOMO (the highest occupied molecular orbital) with respect to the LUMO (the lowest unoccupied molecular orbital) of the dopant.[5]

Recently, several groups have achieved higher σ of donor-donor (D-D) based *p*-type polymers such as poly(3-hexylthiophene) (P3HT) and poly(2,5-bis(3-alkylthiophen-2-yl)thieno[3,2-b]thiophene) (PBTTT) by implementing polymer design strategies such as modification of the backbone electronic structure[6] and side-chain engineering.[7] Film processing methods such as sequential processing (SqP),[8,9] direct dopant evaporation on polymer films[10,11,12] and mechanical rubbing[13] to induce favorable microstructural orientation or ion-exchange methods were also beneficial.[14,15] Leclerc *et al.* incorporated an ether functionality (n-C_7OC_4) in the side-chain of PBTTT and obtained air stable materials with high σ, and PF ~2.9 mW m^{-1} K^{-2} in the chain direction, utilizing films oriented by high temperature rubbing.[16] The polymer p($g_4$2T-T) was functionalized with oligo ethylene oxide side-chains, which enabled polymer-dopant co-processing and aided thermal stability.[17] Even with weak dopants such as DDQ, high σ of ~100 S cm^{-1} was attainable, compared to conventional polythiophenes such as P3HT or PBTTT.[17] Katz *et al.* reported modified PQT12 derivatives by side-chain engineering to achieve σ as high as 350 S cm^{-1} and PF ~12 μW m^{-1} K^{-2}.[18] Patel *et al.* showed that favorable interactions between dopant and polymer side-chains in two polythiophene derivatives (poly(3-(methoxyethoxyethoxy)thiophene) and (poly(3-(methoxyethoxyethoxymethyl)thiophene) led to σ ~37 S cm^{-1}.[19] Reynolds *et al.* reached σ ~250 S cm^{-1} with $AgPF_6$-doped thiophene-dioxythiophene polymers to attain PF of 7 μW m^{-1} K^{-2}.[20] Brinkmann *et al.* demonstrated the role of orientation and microstructural dimensionality in semicrystalline P3HT to achieve σ of 3000 S cm^{-1} and PF of 170 ± 30 μW m^{-1} K^{-2} along the polymer chain direction.[21] A high PF ~120 μW m^{-1} K^{-2} was obtained for the PBTTT:F_4TCNQ system by appropriate control of film morphologies and domain alignment.[22] A conclusion from all this activity is that, without implementing special film-processing techniques to improve macrostructural alignment[13,23] or morphology control,[24,9] the enhancement in σ available by doping is almost always limited, restricting opportunities for further PF improvement in conventional polymeric semiconductors such as P3HT and PBTTT.

To overcome this bottleneck, donor–acceptor (D–A) polymers are being explored as potential candidates for high thermoelectric performance because of their strong solid-state π-π stacking[25] and large persistence lengths that correlate with increased solid-state microstructural order and high charge-carrier mobility.[26] D-A based copolymers offer a wide range of electronic and microstructural tunability to allow excellent charge transport while simultaneously possessing energetic disorder that allows them to achieve a delicate balance

between σ and S. In D-A systems, the energetic separation between Fermi level and transport level often increases, thereby increasing the Seebeck coefficients (S).[27] This has spurred recent attempts to incorporate electron-attracting functional groups in the polymer backbone that increase electron density to achieve high σ, while retaining sufficient energetic disorder to maintain high S values. Cho *et al.* demonstrated a high PF of 276 μW m^{-1} K^{-2} in a DPP-thiophene based polymer versus P3HT that shows ~50 μW m^{-1} K^{-2}.[28] Zhu *et al.* obtained PF ~300 μW m^{-1} K^{-2} in a DPP-based polymer by incorporating the more electron-donating Se atom.[29] Li *et al.* intentionally introduced structural defects in a series of random copolymers with varying fractions of donor-donor block, while simultaneously employing glycol side-chains.[30] This approach raised S while maintaining high σ to obtain high PF. Recently, side-chain engineering using oligo (ethylene glycol) (OEG) based side-chains have gained tremendous importance due to higher polarizability, aiding the stabilization of dopant and polymer ions. This also provides high free volume for dopant accommodation, thereby enhancing the doping efficiency and miscibility of dopant with polymers.[31] OEG-based side-chains exhibit more flexibility than alkyl chains, impart improved ion-conductive behavior, and the capability to coordinate with cations.[32] OEG side-chains can lead to good polaron delocalization due to effective counterion screening.[33,34] OEG groups can promote undesirable ionic conductivity leading to unstable, transient currents.[35] For higher σ, stronger electronic coupling between polymer chains and connectivity between neighbouring crystallites are important. This can be achieved by optimizing the number density of hydrophobic and amphiphilic side-chains in the hydrophobic backbone to enable both interchain interactions and electrostatic screening.

Combining the above research findings, we were motivated utilize the *donor-acceptor approach*, using diketopyrrolopyrrole (DPP) as the acceptor chromophore to obtain an enhancement in the value of seebeck coefficient S. Alongside the need to increase the value of S, it is also important to achieve an enhancement in the value of electrical conductivity σ by incorporating the appropriate amount of electron-donating chromophores in the polymer backbone or electron-donating side chains in conjugation with the polymer skeletal backbone. In keeping with the above design principles, we synthesized four donor-acceptor copolymers by polymerizing diketopyrrolopyrrole and its derivatives containing three different types of donor chromophores: ethylenedioxythiophene (EDOT), thieno [3, 2-b] thiophene and 3,3'-bis (2-(2-(2-methoxyethoxy) ethoxy) ethoxy)-2,2'-bithiophene segments (**Figure 1**). As discussed before, ethylenedioxythiophene (EDOT), thieno [3, 2-b] thiophene and 3,3'-bis (2-(2-(2-methoxyethoxy) ethoxy) ethoxy)-2,2'-bithiophene promote facile hole generation, and generate

effective π-π stacking in the solid-state. At the same time, inclusion of a high number density of OEG or MEET groups can cause the polymer to become increasingly amphiphilic, which can result in transient currents due to ionic conductivity and phase segregation between polymer and dopant resulting in low miscibility.[31-35] Thus, a delicate balance of the number density of amphiphilic glycol-based side-chains and branched hydrophobic side-chains is important for combining efficient charge transport and molecular doping.[36,37,38] The polymers were doped with F_4TCNQ, a synthesized [3]-radialene-based dopant labelled as $Cp(CN)_3$-$(COOMe)_3$ in this study, and a sulfonic acid CF_3SO_3H (**Figure S1, SI**). F_4TCNQ has become a standard *p*-dopant for polymers, including thiophene and DPP polymers,[39,40,41]although its utility with oligoether side-chains may be limited.[42] The radialene dopant has about 0.4 eV greater driving force for *p*-doping than does F_4TCNQ [43,44,45,46] and would be a geometrical contrast (threefold rotational in one isomeric form versus twofold inversion) with F_4TCNQ. CF_3SO_3H presents H^+ as the doping species instead of an organic acceptor, and while used less frequently as a dopant than other sulfonic acids, especially polystyrene sulfonic acid, it has been reported to show unusually high PF with poly(ethylenedioxythiophene).[47] Since the ability of acids to dope conjugated polymers increases with their acid strength, we chose to work with CF_3SO_3H with pK_a values <0.[48] Recently, it has been shown that conjugated electronegative functionalities can effectively stabilize the central 3-membered cyclopropenium ring. This also allows for novel synthetic modifications to tailor the electron affinity and the processability of the dopant.[49,50]

Our key findings are summarized as follows:

- The highest σ ~700 S/cm was exhibited by **P4** on doping with CF_3SO_3H. For the other polymers in this study, σ ~ 300-600 S cm^{-1} and the corresponding PFs were up to 300 μV m^{-1} K^{-2} , among the highest achieved by a single solution blends of homopolymers of symmetrically substituted repeat units.
- The highest σ value, from **P4**, was associated with its having the lowest oxidation potential determined by cyclic voltammetry (CV).
- Our polymer films exhibit considerable air and thermal stability when doped with F_4TCNQ, CF_3SO_3H, $Cp(CN)_3$-$(COOMe)_3$, lasting on the order of 6 weeks.
- We established the mechanism of electrical conductivity by monitoring the source-drain current with respect to time and also by transient thermo-voltage. Unlike PEDOT-based compositions, the doping mechanisms were predominantly electronic.

The highest charge density ~10^{21} cm^{-3} was also obtained for (**P4**) on doping with CF_3SO_3H. Charge density was determined by multiple self-consistent techniques. Thin film morphological characterization by SEM-EDS studies and x-ray diffraction studies confirmed

that the three dopants cause only minute changes in the solid-state aggregation patterns. Infrared (IR) spectroscopies were used to quantify the structural and electronic changes on doping and the mode of polymer-dopant interactions.

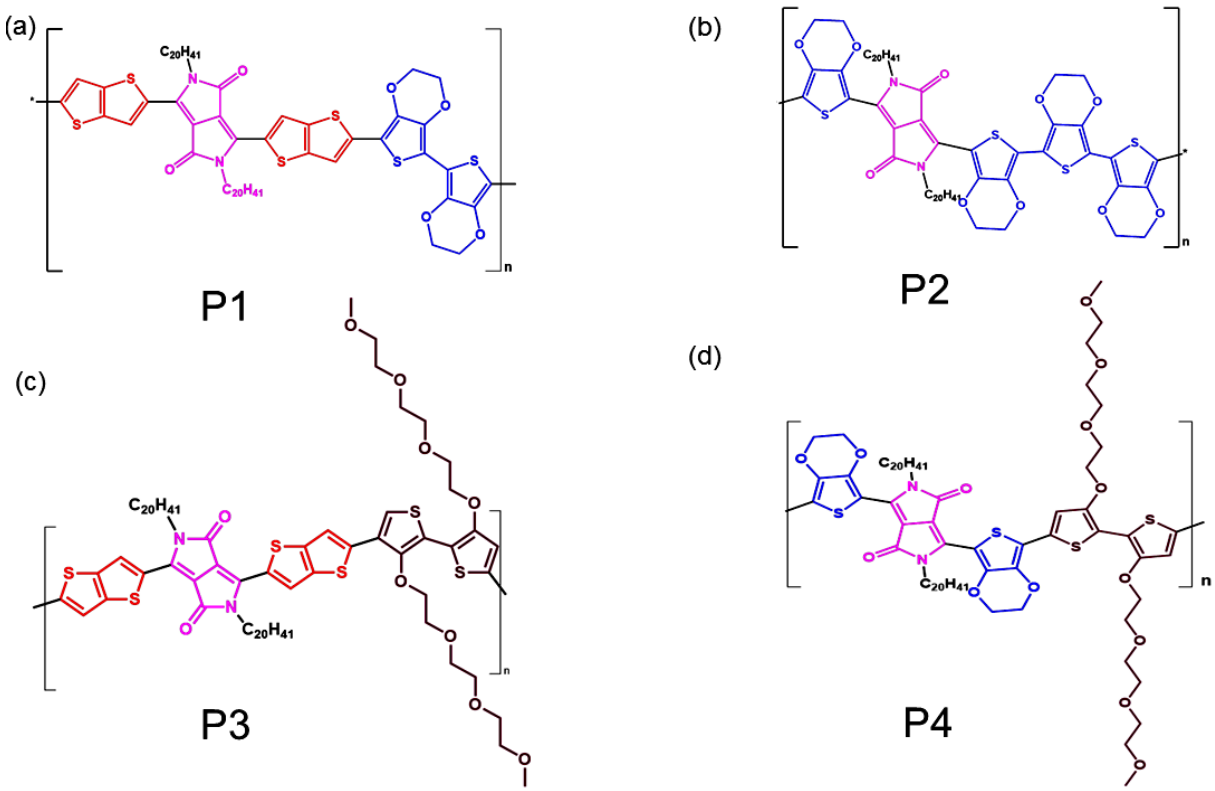

Figure 1. Structures of four polymers studied in this work

2. Results and Discussions

2.1. Synthesis of polymers and dopants

The synthetic scheme of the polymers **P3** and **P4** is shown in **Scheme 1, SI**. The synthesis and chemical characterization of **P1** and **P2** have already been shown in our previous study. The polymers were purified by extensive extraction and reprecipitation, as described in the **SI**. The dopant $Cp(CN)_3$-$(COOMe)_3$ was synthesized using a reported method.[43] The structures of the radialene-based dopant and the newly synthesized polymers (**P3 and P4**) were established by ^{1}H NMR spectroscopy (**Figure S2-S4, SI)** and the polymer polydispersities by gel permeation chromatography (GPC) (**Figure S5-S6, SI**). The GPC traces were dominated by a single high molecular weight peak for each polymer. The molecular weights and PDI values are tabulated in **Table S1, SI**. DSC thermograms of the polymers **P3** and **P4** are shown in **Figure S7, SI.** We obtained those of **P1** and **P2** in our previous work.[51] Broad endotherms

were observed, corresponding to melting above ~120 °C and ~200 °C for **P3** and **P4,** respectively. The highest melting point was found for **P4** among all polymers in the series, implying high crystallinity arising from strong intermolecular attraction.

2.2. Frontier orbital energy levels

Electron density isocontours of HOMO and LUMO of the repeat units of the polymers were obtained by density functional theory (DFT) using a B97-D3 functional and def2-TZVP basis set; (**Figure 2**).[51] Goerigk and Grimme recommend the B97-D3 functional (GGA) for a fairly accurate description of molecular energies,[52] and the def2-TZVP basis set was chosen as a compromise between computational accuracy and cost. We conducted geometry optimization of the repeat units shown in **Figure 1 (a)** and **(e)**, allowing *cis* and *trans* isomers to be explored with respect to rotations about the C-C single bonds linking TT to DPP. It is known that the electrical performance of conjugated polymers has a close relationship with their backbone conformation,[53] with a greater degree of polymer coplanarity corresponding to a desirable enhanced charge transfer capability. Specific to the TT units surrounding DPP, Jackson *et al.* identified a 6 kcal/mole energy barrier associated with rotating a TT unit attached to a DPP unit (the same configuration as described in this paper, [54] and Yu *et al.* quantified a ~1.5 kcal/mole enthalpic preference for the non-traditional C-H…N hydrogen bond over the O…S sulfur bond.[55] We have corroborated both these results. We acknowledge that the DFT methods used in this study probably overestimate the planarity of the structures due to an inherent self-interaction error present in the calculation formalism.[54] To mitigate such a bias would require conducting coupled cluster calculations, which were computationally infeasible due to their very considerable resource requirements. With that said, the calculated HOMO isocontours indicate a more planar configuration in the singlet excited state, and are greatly delocalized throughout the backbone over the DPP as well as the EDOT units. The LUMO isocontours in **Figure 2** demonstrate a decrease in delocalization, which is expected behavior. This leads to an intramolecular charge transfer, thereby inducing a quinoidal character in the polymer backbone. A small degree of EDOT and MEET O-atom conjugation is also seen in the electron density isocontours. This in consistent with previous studies, wherein oxygen atoms in the side-chain that were directly conjugated with the main backbone increased HOMO energy levels.[56,57] Further computational details are given in the SI.

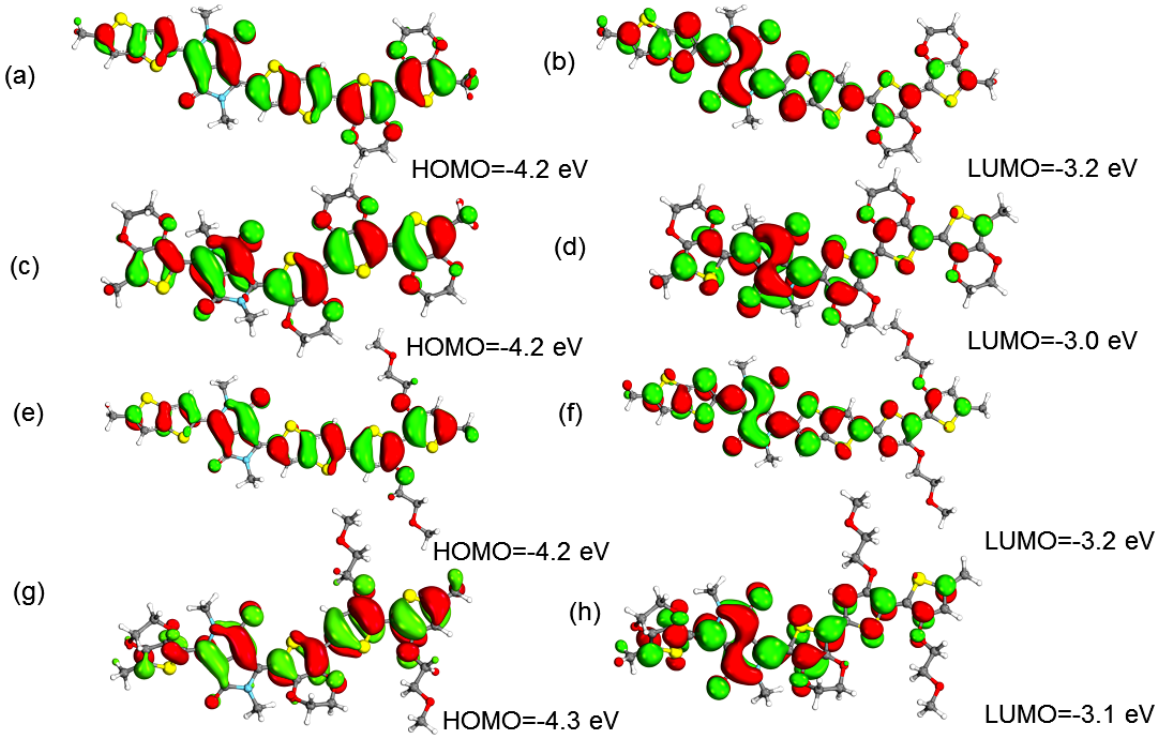

Figure 2. Highest Occupied Molecular Orbital (HOMO) maps from DFT of (a) **P1** (c) **P2** (e) **P3** (g) **P4** and Lowest Unoccupied Molecular Orbital (LUMO) maps of (b) **P1** (d) **P2** (f) **P3** and (h) **P4**. Here, **P1**: p-DPP(TT)$_2$-(EDOT)$_2$) (b) **P2**: p-DPP(EDOT)$_2$-(EDOT)$_2$ (c) **P3**: p-DPP(TT)$_2$-(MEET)$_2$ (d) **P4**: p-DPP(EDOT)$_2$-(MEET)$_2$

Normalized UV-vis spectra in solution and thin films are compared in **Figure 3**. In solution, the polymers exhibit broad absorption over 300 to about 1000 nm with one prominent peak from 500 to about 1000 nm. Film spectra show additional broad absorbance out to 1600 nm that could indicate adventitious doping by the atmosphere.

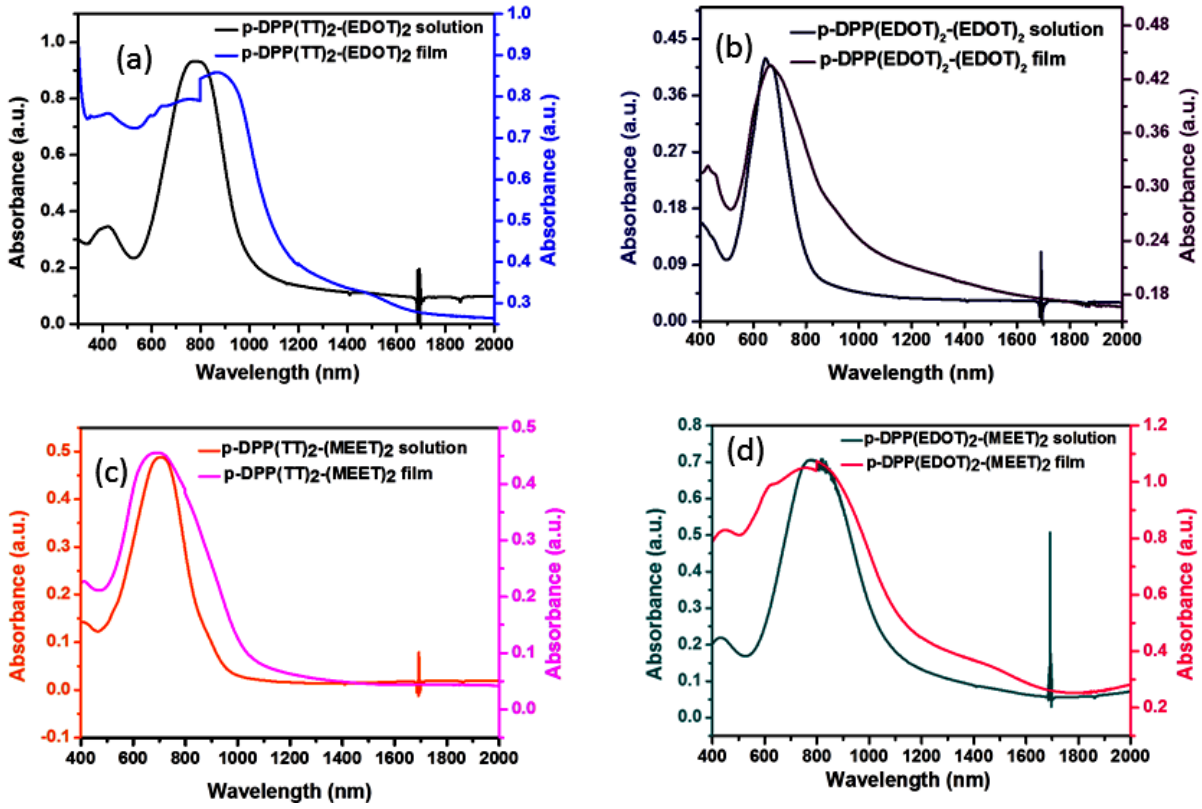

Figure 3. Steady-state UV-visible spectra in solution and thin films of the polymers

The optical gaps, from thin film absorption onsets, are ~0.90 eV. Compared to polymers with thiophene-based donors in DPP-based polymers,[58, 59, 60] the incorporation of an O atom in direct conjugation with the thiophene units causes an increase in the internal donor strength. This imparts a stronger intermolecular charge transfer (ICT) character to the polymer backbone resulting in low optical gaps.[61] Compared to their absorption spectra in solution, polymer films exhibit slightly broader and bathochromically shifted features, consistent with strong intermolecular interactions and longer effective conjugation length [62] in the solid-state as a result of the strong polarity of the DPP lactam units.[63] Doped film spectra are discussed later, in the "polymer doping and induced charge carriers" section.

Cyclic voltammograms of the polymers are depicted in **Figure S8, SI** and the energy gaps are provided in **Table S2, SI**. This Table summarizes the HOMO energies of the polymers extracted from the onset of the oxidation process in the cyclic voltammograms (positions are indicated by grid lines and arrows) and the LUMO energies evaluated utilizing the optical gaps and the HOMO energies from CV studies. The polymers do not exhibit any pronounced activity in the negative potential window, rendering it difficult to otherwise calculate the LUMO values from the voltammograms. The DFT energy level determinations differ from the electrochemical ones in that the DFT calculations were performed on single segments in the gas phase, while the electrochemistry was performed on polymers in solvents, relative to a solvated external

reference, and versus an internal reference reported to have a several tenths of volt range of energies vs. the vacuum level. While the DFT HOMO energies were similar, the electrochemistry indicated that the polymer **P4** exhibits the least positive value of the onset of the oxidation potential, while **P1** exhibits the most positive or the most negative oxidation potential amongst all polymers in this study, indicating that **P4** is the easiest to oxidize and the most capable of stabilizing hole carriers.

Table S2, SI also shows the comparison of the frontier energy levels from CV and DFT studies. We observed a systematic decrease in HOMO energy levels of the polymers in the order **P4** < **P3** < **P2** < **P1**. The LUMO is the deepest for **P1** and the least deep for **P4**. MEET is associated with the least positive onset voltages for oxidation and TT is associated with more positive voltages, with MEET having the stronger effect based on the behavior of **P3**. The calibrating redox potential of Fc/Fc^+ was assumed to be -5.12 eV with respect to vacuum.[64]

2.3. Polymer film morphology

X-ray diffraction of the neat and doped films gave information about microstructures after doping (**Figures 4** and **5**). Diffraction peaks (h00) corresponding to lamellar packing and π-π stacking distances exhibited changes on addition of dopant to the polymer film (50 mol %). To compare the changes in relative crystallinity of the films, we summarized the *d*-spacing corresponding to the (h00) peaks before and after the doping process in **Table S3, SI**. Doping reduces the degree of solid-state aggregation and ordered molecular packing. This can be seen from the broadened peaks and increased *d*-spacings on dopant incorporation/encapsulation into the polymer matrix. An increase in peak width (broadening) along with the reduction in intensities accompanying the dopant addition process is indicative of the decrease of stacking regularity. Although the strong interchain interactions are attenuated by all the dopants, the nature of aggregation varies substantially for each of the dopants, and every dopant affects the *d*-spacings to a different extent. In this study, CF_3SO_3H caused the most disruption of the solid-state packing and aggregation, as seen by the greater loss of certain (h00) peaks. In particular, **P4** with CF_3SO_3H, despite being the best performing composition as will be seen later, shows virtually no long-range crystallinity, consistent with the high compatibility of the side chains and dopant. However, short-range order is still possible in this system.

Aggregation in the neat as well as in the doped polymer films (discussed more fully in the next section) and the extent of phase separation in the doped polymer films were probed by the SEM-EDS studies (**Figure S9, SI** for the dopants, **Figure S10, SI** for the neat and doped polymer films). We carried out elemental analysis at different regions of the scanned area of

the films to quantify the nature of microstructures formed as a result of incorporation of the dopant molecules within the polymer (**Figure S10, SI**) employing the EDS technique. Changes in elemental composition due to the formation of polymer: dopant complexes, as obtained from EDS analysis by monitoring the S: F and S: N ratios are collected in **Table S4, SI**. The

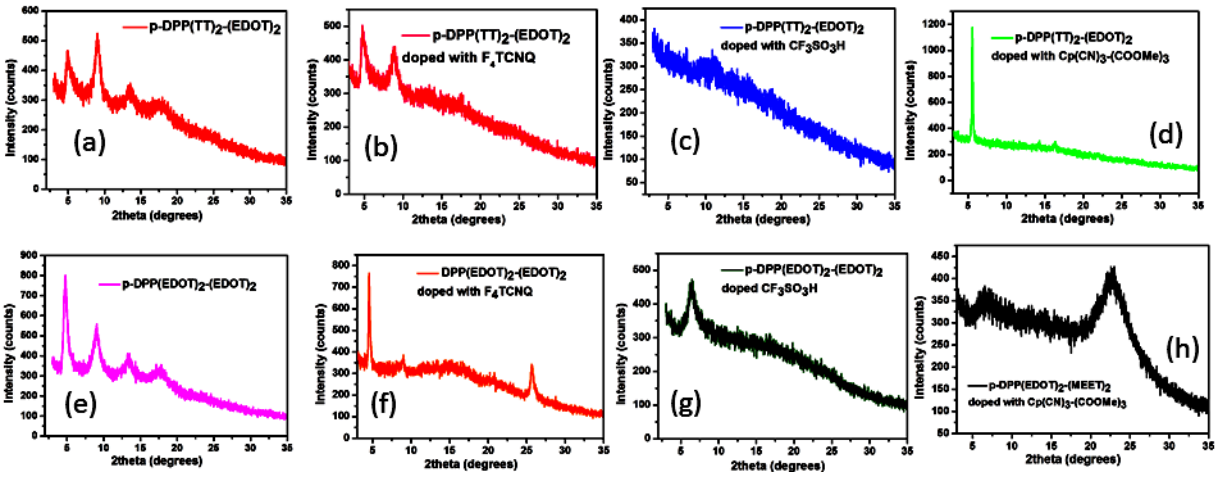

Figure 4. Thin film x-ray diffraction study of p-DPP(TT)$_2$-(EDOT)$_2$ (a) neat film (b) doped with F_4TCNQ (c) doped with CF_3SO_3H (d) doped with Cp(CN)$_3$-(COOMe)$_3$. Corresponding studies for p-DPP(EDOT)$_2$-(EDOT)$_2$ (e) neat film (f) doped with F_4TCNQ (g) doped with CF_3SO_3H and (h) doped with Cp(CN)$_3$-(COOMe)$_3$. Concentration of dopant with respect to polymer: 50 mol %.

morphology change of the polymer and the thin-film aggregates on doping is greatly impacted by the miscibility of the polymer and dopant.

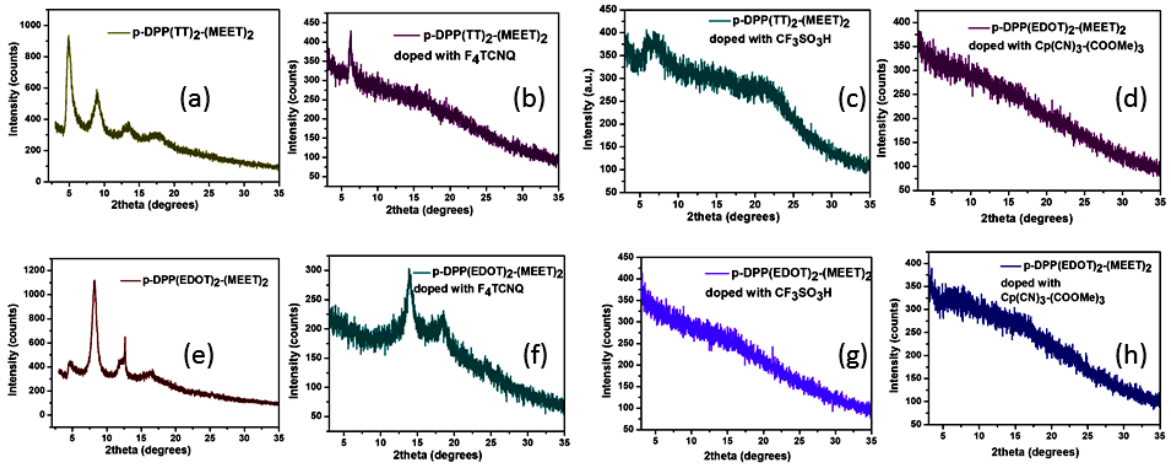

Figure 5. Thin film x-ray diffraction study of p-DPP(TT)$_2$-(MEET)$_2$: (a) neat film (b) doped with F_4TCNQ (c) doped with CF_3SO_3H (d) doped with Cp(CN)$_3$-(COOMe)$_3$. Corresponding for p-DPP(EDOT)$_2$-(MEET)$_2$: (e) neat film (f) doped with F_4TCNQ (g) doped with CF_3SO_3H and (h) doped with Cp(CN)$_3$-(COOMe)$_3$. Concentration of dopant with respect to polymer: 50 mol %.

When polymers are doped with F_4TCNQ and CF_3SO_3H, we observed that the ratio of the percentage composition of the elements S:F is reasonably similar/uniform at all points of analysis for each film, implying negligible or very low extent of phase separation arising from good polymer-dopant miscibility and efficient/homogeneous doping. In some regions, a slightly higher F:S ratio/lower S: F ratio may imply some probability of some phase separation or dopant clustering. Since the dopant $Cp(CN)_3$-$(COOMe)_3$ does not contain F atoms, we have summarized the signal:noise ratios for the polymer films doped with $Cp(CN)_3$-$(COOMe)_3$. Also, the neat polymer films exhibit particle-like morphology while the neat dopant films exhibit a flake-like and a fibre-like morphology (for F_4TCNQ and $Cp(CN)_3$-$(COOMe)_3$, respectively), while the CF_3SO_3H films are featureless, indicating homogeneity that could be beneficial for conductivity. Comparing the morphology of the doped films with those of the neat polymer films or dopant films, we observed that the nature of the aggregates in the doped films does not fully resemble either, which confirms the efficient mixing process, already validated by the x-ray diffractograms.

2.4. Polymer doping and induced charge carriers. Polymer doping was evaluated by Electron Paramagnetic Resonance (EPR) spectroscopy at the same dopant concentration (50 mol % dopants) (**Figure 6).**

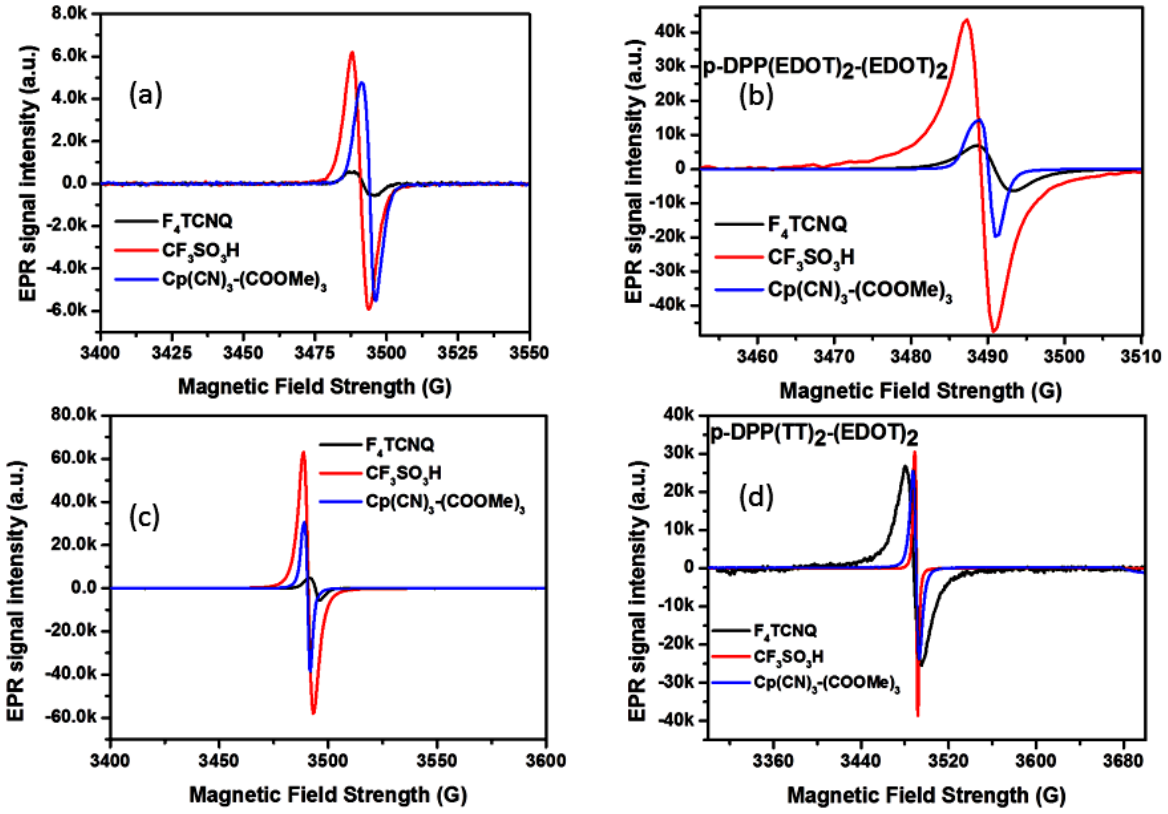

Figure 6. EPR spectra of (a) p-DPP(TT)$_2$-(EDOT)$_2$ **(P1)** (b) p-DPP(EDOT)$_2$-(EDOT)$_2$ **(P2)** (c) p-DPP(TT)$_2$-(MEET)$_2$ **(P3)** and (d) p-DPP(EDOT)$_2$-(MEET)$_2$ **(P4)** on doping.

Notably, the density of radical cations is highest for the CF_3SO_3H dopant, followed by $Cp(CN)_3$-$(COOMe)_3$ and F_4TCNQ. We observed a clear EPR signal, indicating formation of the paramagnetic radical species. We used this signal intensity as a measure of induced polaronic charge. In Figure 6, we observed that at 50 mol % concentration of all dopants (F_4TCNQ, $Cp(CN)_3$-$(COOMe)_3$, CF_3SO_3H, the EPR signal intensity, approximately, follows the order : EPR signal intensity (CF_3SO_3H)>EPR signal intensity ($Cp(CN)_3$-$(COOMe)_3$)>EPR signal intensity (F_4TCNQ). This implies that the dopant CF_3SO_3H produces the highest number density/concentration of polarons compared to F_4TCNQ or $Cp(CN)_3$-$(COOMe)_3$.

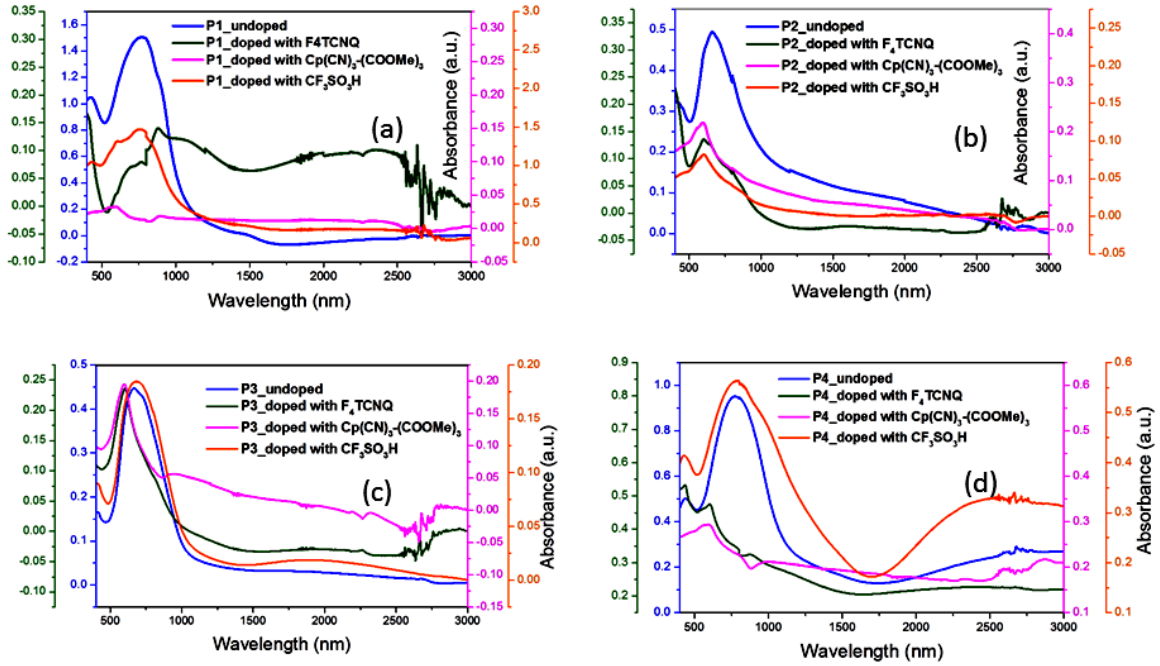

Figure 7. UV-visible spectra of (a) P1 (b) P2 (c) P3 (d) P4 on doping with F_4TCNQ, CF_3SO_3H and $Cp(CN)_3$-$(COOMe)_3$. P1: p-DPP$(TT)_2$-$(EDOT)_2$, P2: p-DPP$(EDOT)_2$-$(EDOT)_2$, P3: p-DPP$(TT)_2$-$(MEET)_2$ and P4: p-DPP$(EDOT)_2$-$(MEET)_2$.

The UV–vis–NIR absorption spectra of the neat and doped polymer films are depicted in **Figure 7**. The signature of *p*-doping of polymers p-DPP$(TT)_2$-$(EDOT)_2$ (P1), *p*-DPP$(EDOT)_2$-$(EDOT)_2$ (P2) and p-DPP$(TT)_2$-$(MEET)_2$ (P3) in their UV-visible spectra is the bleaching of neutral π–π* transition absorption in the range of 500-1000 nm, accompanied by the appearance of new polaronic absorption bands. The additional broad absorption peak and tailing at higher wavelengths can also be associated with a more extended excited state wave function via combination of enhanced π–π stacking and increased co-planarity of the polymer main chain.[65] The solid-state aggregation in thin films may be affected by the viscosity of solvents from which the films are spun;[66] additionally, the assembly and conformation in the solid-state are profoundly determined by the interaction of their side-chains.[67] The higher-wavelength broad absorbance has also been associated with bipolarons in EDOT polymers.[68] The essentially blank EPR spectra of neat **P2** and **P4** (**Figure S11, SI**) helps rule out adventitious doping of the neat polymer films. Due to the strong absorption overlap of polarons and charged F_4TCNQ, [31] it is difficult to evaluate and quantify the degree of charge transfer from steady-state UV-visible spectroscopy, unlike in our previous work.[58]

Therefore, we employed solid-state Fourier transform infrared (FTIR) spectroscopy to evaluate the degree of charge transfer (**Figure S12-S14, SI**). Not only is the C≡N stretch frequency highly sensitive to changes in the local Coulombic environment of the polymer, but

the frequency is near 2200 cm^{-1}, an IR spectral window where other vibrational modes are largely absent. Neutral F_4TCNQ has a vibration mode near 2227 cm^{-1}, while fully anionic species due to the doping process (ICT) undergo mode-softening to ~2190 cm^{-1}.[69]

The placement of dopants within the lamellae, where they reside far from the polymer backbone, leads to integer charge transfer (ICT) complexes. Partial charge transfer (CTC) states only occur when the F_4TCNQ dopant is able to π-stack with the conjugated polymer, thereby involving insufficient wave function between the donor (polymer) and acceptor (dopant).[70] Since the CTC polymorph requires π-interactions between the dopant and polymer, it is kinetically difficult to achieve in crystallites. Thus, ICT is kinetically and thermodynamically favored for the dopant and conjugated polymer system as a whole.[71]

The F_4TCNQ stretching vibrational energy associated with CTCs appears at intermediate stretching frequencies just above 2200 cm^{-1}. It is thus possible to quantitatively extract information from the IR spectra about the overall doping level and/or the ratio of ICT to CTC carriers for each set of processing conditions. The ratio of the integrated infrared peak areas for the CTC peak to that of the central ICT infrared band located near ~2190 cm^{-1} helps quantify the two phases or polymorphs.[72] The ratio of ICT:CTC polymorphs are 1.25, 1.33, 6 and 8 for p-DPP$(TT)_2$-$(EDOT)_2$ (**P1**), p-DPP$(EDOT)_2$-$(EDOT)_2$, (**P2**) p-DPP$(TT)_2$-$(MEET)_2$ (**P3**), and p-DPP$(EDOT)_2$-$(MEET)_2$ (**P4**), respectively, on doping with F_4TCNQ. In our study, we observed that the relative quantity of ICT to CTC in the doped polymer films (50 mol % of F_4TCNQ) follows the order P4>P3>P2>P1. From the solid-state structural perspective, this explains the highest conductivity of P4 amongst all polymers in this series on doping with F4TCNQ.For the two MEET polymers, the reduction in the peak intensities of neutral F_4TCNQ is more drastic, implying more doping. The low polarizability of the polymer backbones poorly screens the interaction between charge carriers on the polymer backbone and the dopant counter-anions. When the dopant counterion in a crystallite is located among the polymer side-chains, it is distant from the holes on the polymer backbone, allowing the holes to become more mobile. This helps explain the trends in electrical conductivity of the doped films of the polymers whereby **P4** exhibits the best performance. **Figure S13, SI** depicts the infrared spectra of the polymers on doping with CF_3SO_3H. The evolution of the –OH group in the $–SO_3H$ group in the polymer IR spectrum (3000-3500 cm^{-1}) indicates the successful integration of the acid dopant into the matrix of the polymer. For $Cp(CN)_3$-$(COOMe)_3$, the neutral absorption peak of –CN group (shown in black) is shifted to lower/softened energies as a result of the doping

process. This shift is a maximum for p-DPP(EDOT)$_2$-(MEET)$_2$ (P4), as depicted in **Figure S14, SI**.

Even more detailed information is available from Raman spectroscopy. As a brief example, we have only shown the structural changes in polymer **P4** have been mapped by Raman spectroscopy, as a representation of doping process by the F_4TCNQ and Cp(CN)$_3$-(COOMe)$_3$ dopants. Subtle differences in the Raman spectra of films of neat and doped polymer films in terms of Raman shifts, line-shapes, widths, broadening, *etc*., were taken into account by Principal Component Analyses with two components. For **P4**, the nature of the Raman spectra on doping with F_4TCNQ, CF_3SO_3H and Cp(CN)$_3$-(COOMe)$_3$ could be distinguished by either PC1 or PC2, or both simultaneously (**Figure S15, SI**). These observations support the hypotheses that F_4TCNQ, CF_3SO_3H and Cp(CN)$_3$-(COOMe) exhibit largely different dopant activities that are distinguishable by just one vector and may, or may not, require a second vector for a thorough distinction. Considering the Raman spectra of **P4** in **Figure S15, SI**, the relevant wavenumbers (cm^{-1}) in the regions of interest have been further assigned and elucidated (**Figures S17-S19, SI).** The Raman shift of the strongest Raman active modes from 1000 to 2000 cm^{-1} can be attributed to C=C stretches in the main polymer chain. The theoretical Raman spectra of **P4** polymer is shown in **Figure S20, SI** and the theoretical peak assignments of the conjugated backbone are collected in **Table S5, SI**. It is evident that the bands become broad and are accompanied by a slight shift to higher energies (cm^{-1}) (blue shift) on doping. Usually, a redshift in the C=C vibration indicates that the introduced charge carriers are mainly polarons at that particular doping level, while broadening of the Raman spectrum with an apparent blueshift is considered to be a signature of bipolaron formation.

2.5. Solid state electronic characterizations.

Plots of conductivity, Seebeck coefficients, and the corresponding thermoelectric power factors are shown in **Figure 8** for the highest-conductivty polymer p-DPP(EDOT)$_2$-(MEET)$_2$ (**P4**) and in **Figures S20-S22, SI** for the other polymers. Their conductivities and thermoelectric power factors (PF) obtained using F_4TCNQ, CF_3SO_3H and Cp(CN)$_3$-(COOMe)$_3$ as dopants (50 mol %) are summarized in **Table 1**. The highest conductivity from F_4TCNQ doping, ~375 S cm^{-1}, was obtained for **P3**, from CF_3SO_3H doping, the highest value of ~700 S cm^{-1} was obtained for **P4**; and the highest value from Cp(CN)$_3$-(COOMe)$_3$ doping, ~325 S cm^{-1}, was again obtained for **P4**. **P1** exhibits a power factor >300 μW m^{-1} K^{-2} on doping with CF_3SO_3H and Cp(CN)$_3$-(COOMe)$_3$, which was the highest value we measured in this series; other power

factors were in the inverse order of the conductivities. To the best of our knowledge, this is the highest thermoelectric power factor obtained from single-repeat-unit, symmetrical conjugated polymers by the direct blending method.

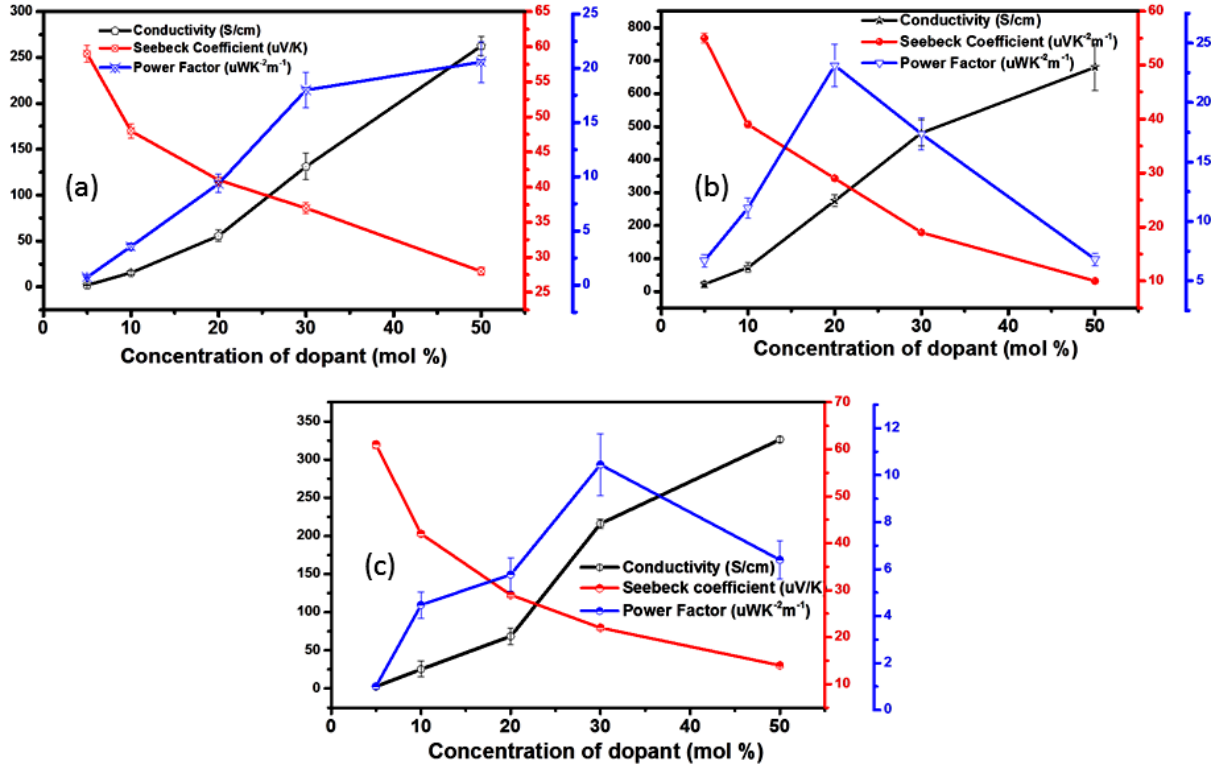

Figure 8. (a) Trends in σ, S, and PF on doping p-DPP(EDOT)$_2$-(MEET)$_2$ (P4) with (a) F_4TCNQ, (b) CF_3SO_3H and (c) Cp(CN)$_3$-(COOMe)$_3$. Connections between points are a guide to the eye.

Table 1. Conductivity (S cm^{-1}) and thermoelectric power factors (PF) (μW K^{-2} m^{-1}) for the four polymers studied with different dopants.

Polymers	F_4TCNQ doping (50 mol %) (σ, PF)	CF_3SO_3H doping (50 mol %) (σ, PF)	Cp(CN)$_3$-(COOMe)$_3$ (50 mol %) (σ, PF)
p-DPP(TT)$_2$-(EDOT)$_2$ **(P1)**	200, 190	250, 190	225, 325
p-DPP(EDOT)$_2$-(EDOT)$_2$ **(P2)**	325, 120	350, 85	320, 200
p-DPP(TT)$_2$-(MEET)$_2$ **(P3)**	375, 65	525, 85	325, 58
p-DPP(EDOT)$_2$-(MEET)$_2$ **(P4)**	275, 20	700, 24	335, 11

In principle, S and σ are strongly and oppositely dependent on the carrier concentration associated with the electronic structure of the materials.[22] This is consistent with a negative

linear correlation with the charge carrier concentration as per the Chabinyc empirical model (**Figure S23-S24, SI**).[73] Again, although the electron affinity of $Cp(CN)_3$-$(COOMe)_3$ is greater than that of F_4TCNQ,[46] σ on doping with $Cp(CN)_3$-$(COOMe)_3$, is only marginally higher than that with F_4TCNQ. This is because morphological aspects such as the degree of dopant incorporation into the polymer, homogeneity of film microstructures and domain alignment often do not directly correspond to the electronic density of states (DOS) and energy-dependent mobility.[74]

σ follows an Arrhenius-type dependence with temperature, T, which can be determined by the equation: $\sigma = \sigma_\infty \exp(-E_a/kT)$, where σ_∞ is the theoretical maximal hole conductivity, k is the Boltzmann constant, T is the temperature and E_a is the thermal activation energy.[75] For temperature-dependent conductivity measurements, we selected the polymer film that incorporated the maximum relative content (~50 mol %) of the dopant. All polymers exhibit a linear dependence of ln(σ) versus reciprocal temperature (**Figure S25-S26, SI**). Values of the thermal activation energy of carrier hopping are shown in **Table 2**; the low magnitudes facilitate higher σ and indicate decreased Coulombic trapping and interdomain barriers. The MEET side-chain conferred lower E_a, consistent with decreased Coulomb trapping because of the higher local polarizability. Microstructural effects such as improved film morphologies, increase in dimensionality or connectivity of domains, shorter inter-aggregate distance or persistence length are expected to reduce the energy barrier for transport in the doped films.[76] The similar and slightly higher values of E_a associated with the organic dopants may be related to transport barriers created by more resistive aggregates, or charge carrier trapping in deeper states in the film implying that greater thermal energy is needed to overcome the barrier.[77] On the other hand, the lower barriers associated with CF_3SO_3H dopant may be the result of the oligoether side-chains being more effective at separating the sulfonate counterions from the hole transport pathways, decreasing the Coulombic interactions between holes and counterions.[78,79]

Table 2. Activation energies obtained from temperature-dependent conductivity measurements (50 mol % doping)

Polymer	E_a for F_4TCNQ (meV)	E_a for CF_3SO_3H (meV)	E_a for $Cp(CN)_3$-$(COOMe)_3$(meV)
p-DPP$(TT)_2$-$(EDOT)_2$ **(P1)**	24.6	16.4	24.4
p-DPP$(EDOT)_2$-$(EDOT)_2$ **(P2)**	20.6	8.1	18.0
p-DPP$(TT)_2$-$(MEET)_2$ **(P3)**	9.6	3.7	8.7
p-DPP$(EDOT)_2$-$(MEET)_2$ **(P4)**	11.6	4.9	7.4

We evaluated the stability of the doped polymer films under ambient and under thermal annealing conditions. All the doped films (with F_4TCNQ and $Cp(CN)_3$-$(COOMe)_3$) in this series lose ~20-30% of the original σ values if left under ambient conditions for six weeks (**Figure 9**). Losses of ~50% occur for **P1** and **P2**), ~30% for **P3** and 20% **P4** when doped with CF_3SO_3H. These ambient stabilities (~60% humidity) are a remarkable improvement as compared to stabilities of polymers reported by Li *et al.* with similar side-chain engineering.[80,81] This degradation of conductivity is affected by the microstructure of the doped films and surface interactions with oxygen and/or water.

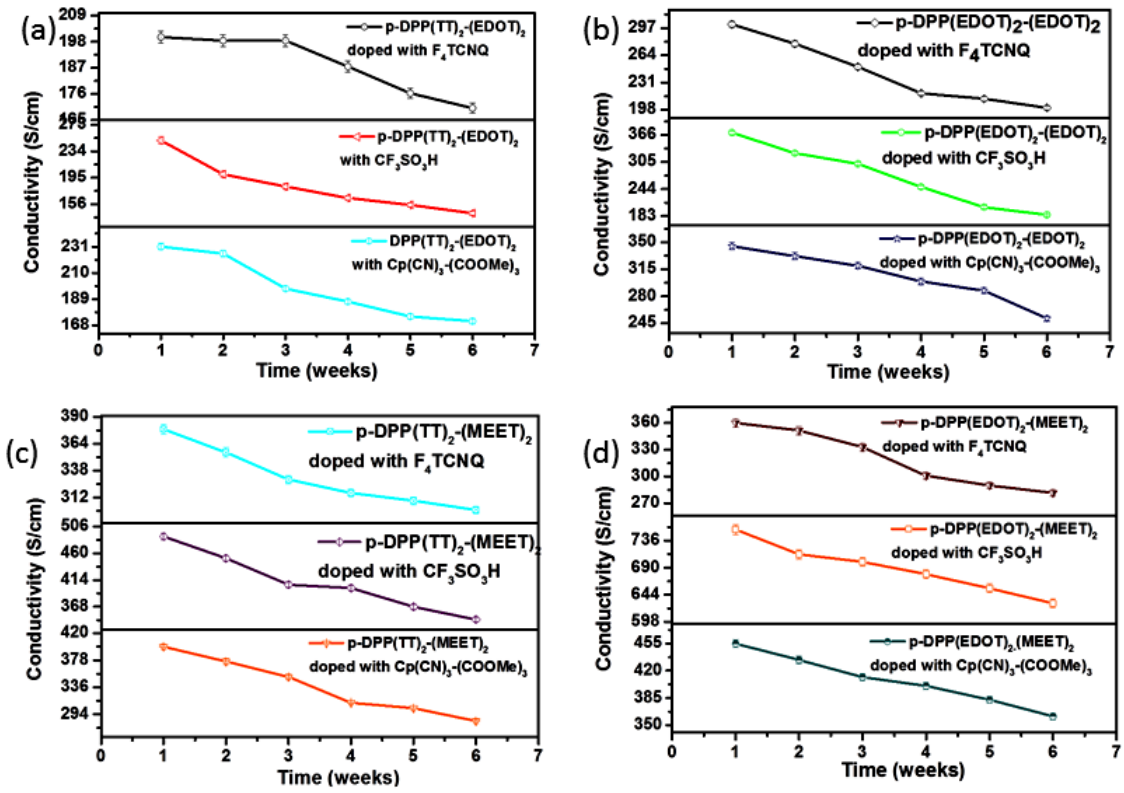

Figure 9. Storage stability of doped films of polymers under ambient, with dopants F_4TCNQ, CF_3SO_3H and $Cp(CN)_3$-$(COOMe)_3$ (50 mol %) (a) DPP(TT)$_2$-(EDOT)$_2$ (b) DPP(EDOT)$_2$-(EDOT)$_2$ (c) DPP(TT)$_2$-(MEET)$_2$ and (d) DPP(EDOT)$_2$-(MEET)$_2$ (50 mol % of dopant).

OEG side-chains can increase hole number density by decreasing the energy of charge separation. However, heating the doped polymer films may cause dissociation of the ion pairs, thereby disrupting the morphology.[17] Thermal stabilities (100°C/1 h) of doped polymer σ are shown in **Figure S27, SI**. F_4TCNQ-doped films of **P3** and **P4** show degradation ~20%, while those of **P1** and **P2** show a degradation of ~30%. The $Cp(CN)_3$-$(COOMe)_3$-doped films show trends similar to the F_4TCNQ-doped films. The CF_3SO_3H-doped non-MEET films show higher degradation, ~50 % for **P1** and **P2**, while CF_3SO_3H-doped MEET films were more stable: only ~10-20% degradation for **P3** and **P4**. On cooling under ambient conditions for ~12 hours, the doped films show impressive recovery, most apparent for **P4**. The ionization energy of **P4** is the lowest compared to other polymers in this series, as seen from CV and DFT calculations, which not only facilitates doping but also lessens hole neutralization. The electron-donating ability of oxygens attached to the thiophene ring stabilizes the doped form, as described before.[17]

To establish the conductivity mechanism, we monitored source-drain current (I_{DS}) over time (**Figure S28, SI**). I_{DS} values are almost constant, with minimal loss of hole current for all dopant-polymer combinations, indicating that the mechanism is predominantly electronic

(**Table S6, SI**). When the polymers are doped with F_4TCNQ and $Cp(CN)_3$-$(COOMe)_3$, the thermoelectric voltages remain constant when measured during applied ΔT intervals; minor instabilities/fluctuations are observed for CF_3SO_3H at each ΔT (**Figure S29, SI**). However, this is different from the transient ΔV induced by ΔT typical of ionic conductivity in PEDOT: PSS.[81] If the conduction mechanism is electronic, a symmetric spike in the thermoelectric voltage should not be observed. This implies a constant flux of holes along the temperature gradient and no accumulations/depletions of ions building up at the electrodes.[82,83]

2.6. Organic Field Effect Transistor (OFET) studies

The transfer and output characteristics of the neat and doped films (0.1 mol % of dopants) of polymers and plots of $I_{DS}^{1/2}$(A) versus V_G (V) are shown in **Figure S30-S33, SI** and **Figure S34, SI**, respectively. **Table S7, SI** summarizes the corresponding threshold voltages and hole mobilities, with **P4** being the highest. The presence of oxygen-bearing side-chains further enables strong aggregation between adjacent polymer segments.[84,85] The progressively more positive threshold voltages on moving from **P1** to **P4** compared to its other counterparts in this series is indicative of lower solid-state trap densities.[86] The addition of only 0.1% of dopants (F_4TCNQ, CF_3SO_3H and $Cp(CN)_3$-$(COOMe)_3$) caused about an order of magnitude enhancement in the charge carrier mobilities. However, addition of 0.1% of F_4TCNQ results in less negative threshold voltages than the neat (undoped) film of the respective polymers, while 0.1% of CF_3SO_3H and $Cp(CN)_3$-$(COOMe)_3$ lead to highly positive threshold voltages. The increased mobility and more positive threshold voltages on doping indicate a decreased density of shallow trap defects, a decrease in trap states at grain boundaries, or a reduction in contact resistance.[87,88]

2.7 Remote-gate platform for doping study

Jang *et al.* developed a method to quantify dopant effects and diffusion in polymers using a remote-gate (RG) field transistor setup. In this setup, the surface potential of the polymer film is monitored by coupling to the oxide gate of a commercial silicon FET in series with a "remote" gate electrode and an acetonitrile (ACN) solution between the electrode and the film.[89,90] The schematic is shown in **Figure S38, SI**.[89,90] We estimated the charge carrier density as a result of doping the polymers with F_4TCNQ, CF_3SO_3H and $Cp(CN)_3$-$(COOMe)_3$. The polymeric sensing layer was spin-coated onto a Si/SiO_2 (300 nm thermal oxide) substrate. Subtle changes in the surface potential of the polymer film are reported via the FET $V_{th,RG}$ shift. The mechanism of interaction between dopant and polymer films dictates the direction and magnitude of this shift.

Figures S35 and S36, SI display the transfer curves of the RG FET coupled with our responsive polymer layers. Initially, the baseline $V_{th,RG}$ is obtained when the polymer film is equilibrated with neat ACN. After that, we add a drop (30 µL) of each concentration (in increasing order of concentration of a particular dopant) and then re-measure the RG field effect transistor. For every dopant, we see a horizontal shift to the left towards lower threshold voltages. This is a consequence of additional positive interfacial potential on the polymeric film relative to that of the solution compared to that using neat ACN, a consequence of induced holes in the polymer layer and counterions closer to the ACN. **Figure 10** represents the variation of $V_{th,RG}$ with 10 consecutive scans at each dopant concentration in the ACN. Only slight drifts are observed once each solution has equilibrated with the films.

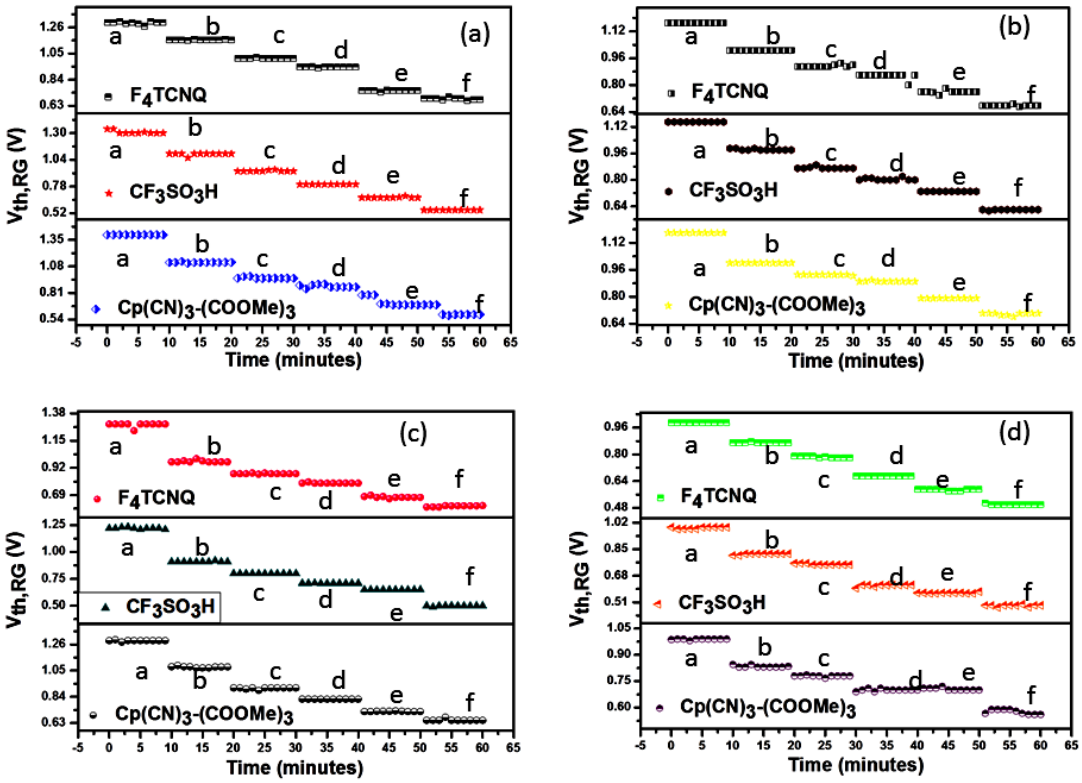

Figure 10. Threshold voltage changes/drifts (corresponding to 1 µA current in the transfer curves) of a commercial silicon transistor as a function of time. For every concentration of the added dopant (mentioned in the inset) in overlying solution, the transfer curves were allowed to stabilize for 10 minutes (~10 cycles) for (a) p-DPP(TT)$_2$-(EDOT)$_2$ (P1) (b) p-DPP(EDOT)$_2$-(EDOT)$_2$ (P2) (c) p-DPP(TT)$_2$-(MEET)$_2$ (P3) (d) p-DPP(EDOT)$_2$-(MEET)$_2$ (P4). The dopant concentrations in acetonitrile are 10-6, 10-4, 0.01, 0.1 and 1 mg/ml.

To extract hole concentration and mobility changes induced by dopants, we can use the equations as in our previous work: [91,92]

$$\sigma = \rho.e.\mu \qquad [1]$$

$$\rho_d = \rho_o \exp(-e\Delta V_{th,RG}/kT) \qquad [2]$$

where σ is defined as the experimental four-point-probe conductivity, μ_h is the hole mobility, and ρ is the carrier concentration (ρ_o and ρ_d are the carrier concentrations without and with doping, respectively). $\Delta V_{th,RG}$ was extracted from the FET transfer curve shift. To calculate the original charge densities (ρ_o), we used the charge densities, ρ_c, calculated by substituting σ values from the four-point conductivity measurements for every concentration of dopant added and the OFET mobility values for 0.1 wt% of dopant added (the highest doping that allowed OFET characterization) from **Table S8, SI** into Equation [1]. The resulting values of ρ_c, *extrapolated to zero dopant concentration*, give ρ_0. Rearranging equation [2] yields

$$\ln\rho_d = \ln\rho_o - e\Delta V_{th,RG}/kT \qquad [3]$$

Fits enabling the extraction of ρ_o (with explanations in the caption) are shown in **Figure S38-S39, SI**. Separately, the charge densities were ~10^{12}-10^{13} cm^{-3} without added dopants (**Table S9, SI**), as obtained from OFET transfer curves. Note that extrapolations to zero dopant concentration are within an order of magnitude of those obtained from OFETs at zero gate voltage. Using values of ρ_0 calculated for each polymer using the extrapolation method, a series of values of charge densities, ρ_d, were obtained for different concentrations of dopant species in the ACN solutions, as shown in **Table S9-S12, SI** for each of our polymers. CF_3SO_3H was capable of generating the highest density of holes, followed by $Cp(CN)_3$-$(COOMe)_3$, and then F_4TCNQ. This is consistent with our 4-probe conductivity studies described in the previous section. The highest charge density ~10^{21} cm^{-3} is obtained for p-$DPP(EDOT)_2$-$(MEET)_2$ which is in agreement with the highest propensity of this polymer to be doped.

3. Conclusions

We have synthesized and analyzed novel polymers based on DPP, EDOT and MEET, and used three dopants including the synthesized dopant $Cp(CN)_3$-$(COOMe)_3$ to achieve exceptionally high hole conductivities while retaining high S, collectively leading to exceptionally high PF ~300 μW m^{-1} K^{-2}. All-electronic conductivity is demonstrated via extended current accumulation tests. Collectively tailoring backbone design and the number density and nature of side-chains led to frontier orbital delocalization and hence low HOMO energies, as

established by CV and DFT studies. Trends in hole conductivity are consistent with electrochemical oxidizability, with **P4** and **P1** showing the highest and lowest conductivies, respectively. UV-visible and IR spectroscopy provided qualitative and quantitative analyses of the degree of charge transfer in the doped polymer films. Combining hydrophobic and polarizable side-chains allows hole transport and dopant miscibility to be simultaneously promoted. It is apparent that the MEET side-chains combined with EDOT rings, by adding electron-donating functionality and local polarizability, increase both hole generation efficiency and mobility for higher hole conductivity.

Supporting Information

Supporting Information is available from the Wiley Online Library or from the author.

Acknowledgements

This work was primarily supported by the National Science Foundation, Division of Chemistry, grant numbers 1708245 and 2107360. The x-ray diffraction and SEM-EDS studies were supported by U.S. Department of Energy, Office of Science, Basic Energy Sciences, Materials Chemistry Program, under Award number DE-FG02-07ER46465. The computational work was carried out at the Advanced Research Computing at Hopkins (ARCH) core facility (rockfish.jhu.edu), which is supported by the National Science Foundation (NSF) grant number OAC 1920103. We are grateful to Nan (Louise) Chen for assistance with calculations and Dr. Christina Kouseff for helpful discussions.

Received: ((will be filled in by the editorial staff))

Revised: ((will be filled in by the editorial staff))

Published online: ((will be filled in by the editorial staff))

References

[1] A. J. Epstein, F. -C. Hsu, N. -R. Chiou, V. N. Prigodin, *Synth. Met.* **2003**, *137*, 859–861. https://doi.org/https://doi.org/10.1016/S0379-6779(02)01091-3.

[2] Y. Wang, Y. -J. Hu, B. Bocklund, S. -L. Shang, B. -C. Zhou, Z. -K. Liu, L. -Q. Chen, *Phys. Rev. B* **2018**, *98*, 224101. https://doi.org/10.1103/PhysRevB.98.224101.

[3] Y. Xu, X. Wang, J. Zhou, B. Song, Z. Jiang, E. M. Y. Lee, S. Huberman, K. K. Gleason, G. Chen, *Sci. Adv.* **2022**, *4*, eaar3031. https://doi.org/10.1126/sciadv.aar3031.

[4] M. Upadhyaya, C. J. Boyle, D. Venkataraman, Z. Aksamija, *Sci. Rep.* **2019**, *9*, 5820.

https://doi.org/10.1038/s41598-019-42265-z.

[5] Q. Bao, X. Liu, S. Braun, F. Gao, M. Fahlman, *Adv. Mater. Interfaces* **2015**, *2*, 1400403. https://doi.org/https://doi.org/10.1002/admi.201400403.

[6] H. Li, M. E. DeCoster, C. Ming, M. Wang, Y. Chen, P. E. Hopkins, L. Chen, H. E. Katz, *Macromolecules* **2019**, *52*, 9804–9812. https://doi.org/10.1021/acs.macromol.9b02048.

[7] Y. Ding, Y. Zhu, X. Wang, Y. Wang, S. Zhang, G. Zhang, X. Gu, L. Qiu, *Chem. Mater.* **2022**, *34*, 2696–2707. https://doi.org/10.1021/acs.chemmater.1c04085.

[8] A. R. Chew, R. Ghosh, Z. Shang, F. C. Spano, A. Salleo, *J. Phys. Chem. Lett.* **2017**, *8*, 4974–4980. https://doi.org/10.1021/acs.jpclett.7b01989.

[9] T. Ma, B. X. Dong, G. L. Grocke, J. Strzalka, S. N. Patel, *Macromolecules* **2020**, *53*, 2882–2892. https://doi.org/10.1021/acs.macromol.0c00402.

[10] M. T. Fontana, D. A. Stanfield, D. T. Scholes, K. J. Winchell, S. H. Tolbert, B. J. Schwartz, *J. Phys. Chem. C* **2019**, *123*, 22711–22724. https://doi.org/10.1021/acs.jpcc.9b05069.

[11] A. I. Hofmann, R. Kroon, L. Yu, C. Müller, *J. Mater. Chem. C* **2018**, *6*, 6905–6910. https://doi.org/10.1039/C8TC01593G.

[12] R. Fujimoto, S. Watanabe, Y. Yamashita, J. Tsurumi, H. Matsui, T. Kushida, C. Mitsui, C.; H. T. Yi, V. Podzorov, J. Takeya, *Org. Electron.* **2017**, *47*, 139–146. https://doi.org/https://doi.org/10.1016/j.orgel.2017.05.019.

[13] L. Deng, G. Chen, *Nano Energy* **2021**, *80*, 105448. https://doi.org/https://doi.org/10.1016/j.nanoen.2020.105448.

[14] Y. Yamashita, J. Tsurumi, M. Ohno, R. Fujimoto, S. Kumagai, T. Kurosawa, T. Okamoto, J. Takeya, S. Watanabe, *Nature* **2019**, *572*, 634–638. https://doi.org/10.1038/s41586-019-1504-9.

[15] J. E. Cochran, M. J. N. Junk, A. M. Glaudell, P. L. Miller, J. S. Cowart, M. F. Toney, C. J. Hawker, B. F. Chmelka, M. L. Chabinyc, *Macromolecules* **2014**, *47*, 6836–6846. https://doi.org/10.1021/ma501547h.

[16] P. Durand, H. Zeng, T. Biskup, V. Vijayakumar, V. Untilova, C. Kiefer, B. Heinrich, L. Herrmann, M. Brinkmann, N. Leclerc, *Adv. Energy Mater.* **2022**, *12*, 2103049. https://doi.org/https://doi.org/10.1002/aenm.202103049.

[17] R. Kroon, D. Kiefer, D. Stegerer, L. Yu, M. Sommer, C. Müller, *Adv. Mater.* **2017**, *29*, 1700930. https://doi.org/https://doi.org/10.1002/adma.201700930.

[18] H. Li, M. E. DeCoster, R. M. Ireland, J. Song, P. E. Hopkins, H. E. Katz, *J. Am. Chem. Soc.* **2017**, *139*, 11149–11157. https://doi.org/10.1021/jacs.7b05300.

[19] B. X. Dong, C. Nowak, J. W. Onorato, T. Ma, J. Niklas, O. G. Poluektov, G. Grocke, M. F. DiTusa, F. A. Escobedo, C. K. Luscombe, P. F. Nealey, S. N. Patel, *Chem. Mater.* **2021**, *33*, 741–753. https://doi.org/10.1021/acs.chemmater.0c04153.

[20] J. F. Ponder Jr., A. K. Menon, R. R. Dasari, S. L. Pittelli, K. J. Thorley, S. K. Yee, S. R. Marder, J. R. Reynolds, *Adv. Energy Mater.* **2019**, *9*, 1900395. https://doi.org/https://doi.org/10.1002/aenm.201900395.

[21] Y. Zhong, V. Untilova, D. Muller, S. Guchait, C. Kiefer, L. Herrmann, N. Zimmermann, M. Brosset, T. Heiser, M. Brinkmann, *Adv. Funct. Mater.* **2022**, *32*, 2202075. https://doi.org/https://doi.org/10.1002/adfm.202202075.

[22] S. N. Patel, A. M. Glaudell, K. A. Peterson, E. M. Thomas, K. A. O'Hara, E. Lim, M. L. Chabinyc, *Sci. Adv.* **2022**, *3*, e1700434. https://doi.org/10.1126/sciadv.1700434.

[23] V. Vijayakumar, Y. Zhong, V. Untilova, M. Bahri, L. Herrmann, L. Biniek, N. Leclerc, M. Brinkmann, *Adv. Energy Mater.* **2019**, *9*, 1900266. https://doi.org/https://doi.org/10.1002/aenm.201900266.

[24] L. Yu, D. Scheunemann, A. Lund, D. Kiefer, C. Müller, *Appl. Phys. Lett.* **2021**, *119*, 181902. https://doi.org/10.1063/5.0075789.

[25] X. Yan, M. Xiong, X. -Y. Deng, K. -K. Liu, J. -T. Li, X. -Q. Wang, S. Zhang, N. Prine, Z. Zhang, W. Huang, *Nat. Commun.* **2021**, *12*, 5723. https://doi.org/10.1038/s41467-021-26043-y.

[26] W. Shi, T. Deng, Z. M. Wong, G. Wu, S. -W. Yang, *npj Comput. Mater.* **2021**, *7*, 107. https://doi.org/10.1038/s41524-021-00580-y.

[27] K. Takeda, *J. Math. Chem.* **1994**, *15*, 323–337. https://doi.org/10.1007/BF01277568.

[28] I. H. Jung, C. T. Hong, U.-H. Lee, Y. H. Kang, K. -S. Jang, S. Y. Cho, *Sci. Rep.* **2017**, *7*, 44704. https://doi.org/10.1038/srep44704.

[29] J. Ding, Z. Liu, W. Zhao, W. Jin, L. Xiang, Z. Wang, Y. Zeng, Y. Zou, F. Zhang, Y. Yi, Y. Diao, C. R. McNeill, C.-a. Di, D. Zhang, D. Zhu, *Angew. Chemie Int. Ed.* **2019**, *58*, 18994–18999. https://doi.org/https://doi.org/10.1002/anie.201911058.

[30] H. Li, J. Song, J. Xiao, L. Wu, H. E. Katz, L. Chen, *Adv. Funct. Mater.* **2020**, *30*, 2004378. https://doi.org/https://doi.org/10.1002/adfm.202004378.

[31] D. Kiefer, R. Kroon, A. I. Hofmann, H. Sun, X. Liu, A. Giovannitti, D. Stegerer, A. Cano, J. Hynynen, L. Yu, Y. Zhang, D. Nai, T. F. Harrelson, M. Sommer, A. J. Moule, M. Kemerink, S. R. Marder, I. McCulloch, M. Fahlman, S. Fabiano, C. Muller, *Nat. Mater.* **2019**, *18*, 149–155. https://doi.org/10.1038/s41563-018-0263-6.

[32] P. Schmode, A. Savva, R. Kahl, D. Ohayon, F. Meichsner, O. Dolynchuk, T. Thurn-

Albrecht, S. Inal, M. Thelakkat, *ACS Appl. Mater. Interfaces* **2020**, *12*, 13029–13039. https://doi.org/10.1021/acsami.9b21604.

[33] S. Sami, R. Alessandri, R. Broer, R. W. A. Havenith, *ACS Appl. Mater. Interfaces* **2020**, *12*, 17783–17789. https://doi.org/10.1021/acsami.0c01417.

[34] J. Brebels, E. Douvogianni, D. Devisscher, R. Thiruvallur Eachambadi, J. Manca, L. Lutsen, D. Vanderzande, J. C. Hummelen, W. Maes, *J. Mater. Chem. C* **2018**, *6*, 500–511. https://doi.org/10.1039/C7TC05264B.

[35] E. M. Thomas, P. H. Nguyen, S. D. Jones, M. L. Chabinyc, R. A. Segalman, *Annu. Rev. Mater. Res.* **2021**, *51*, 1–20. https://doi.org/10.1146/annurev-matsci-080619-110405.

[36] O. Kettner, A. Pein, G. Trimmel, P. Christian, C. Röthel, I. Salzmann, R. Resel, G. Lakhwani, F. Lombeck, M. Sommer, B. Friedel, *Synth. Met.* **2016**, *220*, 162–173. https://doi.org/https://doi.org/10.1016/j.synthmet.2016.06.010.

[37] C. Kanimozhi, N. Yaacobi-Gross, K. W. Chou, A. Amassian, T. D. Anthopoulos, S. Patil, *J. Am. Chem. Soc.* **2012,** *40*, 16532–16535. https://doi.org/10.1021/ja308211n.

[38] S. Ghosh, S. Shankar, D. S. Philips, A. Ajayaghosh, *Mater. Today Chem.* **2020**, *16*, 100242. https://doi.org/https://doi.org/10.1016/j.mtchem.2020.100242.

[39] S. E. Yoon, Y. Kang, S. Y. Noh, J. Park, S. Y. Lee, J. Park, D. W. Lee, D. R. Whang, T. Kim, G. -H. Kim, H. Seo, B. -G. Kim, J. H. Kim, *ACS Appl. Mater. Interfaces* **2020**, *12*, 1151–1158. https://doi.org/10.1021/acsami.9b17825.

[40] S. A. Gregory, J. F. J. Ponder, S. L. Pittelli, M. D. Losego, J. R. Reynolds, S. K. Yee, *ACS Appl. Polym. Mater.* **2021**, *3*, 2316–2324. https://doi.org/10.1021/acsapm.1c00093.

[41] S. A. Gregory, A. K. Menon, S. Ye, D. S. Seferos, J. R. Reynolds, S. K. Yee, *Adv. Energy Mater.* **2018**, *8*, 1802419. https://doi.org/https://doi.org/10.1002/aenm.201802419.

[42] P. A. Finn, I. E. Jacobs, J. Armitage, R. Wu, B. D. Paulsen, M. Freeley, M. Palma, J. Rivnay, H. Sirringhaus, C. B. Nielsen, *J. Mater. Chem. C* **2020**, *8*, 16216–16223. https://doi.org/10.1039/D0TC04290K.

[43] J. Saska, G. Gonel, Z. I. Bedolla-Valdez, S. D. Aronow, N. E. Shevchenko, A. S. Dudnik, A. J. Moulé, M. Mascal, *Chem. Mater.* **2019**, *31*, 1500–1506. https://doi.org/10.1021/acs.chemmater.8b04150.

[44] J. Li, G. Zhang, D. M. Holm, I. E. Jacobs, B. Yin, P. Stroeve, M. Mascal, A. J. Moulé, *Chem. Mater.* **2015**, *27*, 5765–5774. https://doi.org/10.1021/acs.chemmater.5b02340.

[45] J. Gao, J. D. Roehling, Y. Li, H. Guo, A. J. Moulé, J. K. Grey, *J. Mater. Chem. C* **2013**, *1*, 5638–5646. https://doi.org/10.1039/C3TC31047G.

[46] J. Li, I. Duchemin, O. M. Roscioni, P. Friederich, M. Anderson, E. Da Como, G. Kociok-

Köhn, W. Wenzel, C. Zannoni, D. Beljonne, X. Blase, G. D'Avino, *Mater. Horizons* **2019**, *6*, 107–114. https://doi.org/10.1039/C8MH00921J.

[47] C. Wang, K. Sun, J. Fu, R. Chen, M. Li, Z. Zang, X. Liu, B. Li, H. Gong, J. Ouyang, *Adv. Sustain. Syst.* **2018**, *2*, 1800085. https://doi.org/https://doi.org/10.1002/adsu.201800085.

[48] C. C. Han, R. L. Elsenbaumer, *Synth. Met.* **1989**, *30*, 123–131. https://doi.org/https://doi.org/10.1016/0379-6779(89)90648-6.

[49] N. A. Turner, M. B. Freeman, H. D. Pratt, A. E. Crockett, D. S. Jones, M. R. Anstey, T. M. Anderson, C. M. Bejger, *Chem. Commun.* **2020**, *56*, 2739–2742. https://doi.org/10.1039/C9CC08547E.

[50] Y. Karpov, T. Erdmann, I. Raguzin, M. Al-Hussein, M. Binner, U. Lappan, M. Stamm, K. L. Gerasimov, T. Beryozkina, V. Bakulev, D. V. Anokhin, D. V. Ivanov, F. Gunther, S. Gemming, G. Seiffert, B. Voit, R. D. Pietro, *Adv. Mater.* **2016**, *28*, 6003–6010. https://doi.org/https://doi.org/10.1002/adma.201506295.

[51] B. -G. Kim, X. Ma, C. Chen, Y. Ie, E. W. Coir, H. Hashemi, Y. Aso, P. F. Green, J. Kieffer, J. Kim, *Adv. Funct. Mater.* **2013**, *23*, 439–445. https://doi.org/https://doi.org/10.1002/adfm.201201385.

[52] L. Goerigk, S. Grimme, *Phys. Chem. Chem. Phys.*, **2011**, *13*, 6670-6688.

[53] Zi-Di. Yu, Y. Lu, Prof. Jie-Yu Wang, Prof. J. Pei, *Chem. Eur. J.* **2020**, *26*, 16194. https://doi.org/10.1002/chem.202000220.

[54] N. E. Jackson, B. M. Savoie, K. L. Kohlstedt, M. O. de la Cruz, G. C. Schatz, L. X. Chen, M. A. Ratner, *J. Am. Chem. Soc.* **2013**, *28*, 10475–10483 https://pubs.acs.org/doi/full/10.1021/ja403667s

[55] B. Liu, D. Rocca, H. Yan, D. Pan, *J. Am. Chem. Soc.* **2021**, *12*, 2182–2187

[56] B. Meng, J. Liu, L. Wang, *Polym. Chem.* **2020**, *11*, 1261–1270. https://doi.org/10.1039/C9PY01469A.

[57] S. -F. Yang, Z. -T. Liu, Z. -X. Cai, M. J. Dyson, N. Stingelin, W. Chen, H. -J. Ju, G. -X. Zhang, D. -Q. Zhang, *Adv. Sci.* **2017**, *4*, 1700048. https://doi.org/https://doi.org/10.1002/advs.201700048.

[58] T. Mukhopadhyaya, T. D. Lee, C. Ganley, S. Tanwar, P. Raj, L. Li, Y. Song, P. Clancy, I. Barman, S. Thon, H. E. Katz, *Adv. Funct. Mater.* **2022**, *32*, 2208541. https://doi.org/https://doi.org/10.1002/adfm.202208541.

[59] A. Karolewski, A. Neubig, M. Thelakkat, S. Kümmel, *Phys. Chem. Chem. Phys.* **2013**, *15*, 20016–20025. https://doi.org/10.1039/C3CP52739E.

[60] X. Zhao, H. Cai, Y. Deng, Y. Jiang, Z. Wang, Y. Shi, Y. Han, Y. Geng, *Macromolecules* **2021**, *54*, 3498–3506. https://doi.org/10.1021/acs.macromol.1c00124.

[61] M. C. Scharber, N. S. Sariciftci, *Adv. Mater. Technol.* **2021**, *6*, 2000857. https://doi.org/https://doi.org/10.1002/admt.202000857.

[62] H. Meier, U. Stalmach, H. Kolshorn, *Acta Polym.* **1997**, *48*, 379–384. https://doi.org/https://doi.org/10.1002/actp.1997.010480905.

[63] H. Tanaka, A. Wakamatsu, M. Kondo, S. Kawamura, S. Kuroda, Y. Shimoi, W. -T. Park, Y.-Y. Noh, T. Takenobu, *Commun. Phys.* **2019**, *2*, 96. https://doi.org/10.1038/s42005-019-0196-7.

[64] C. M. Cardona, W. Li, A. E. Kaifer, D. Stockdale, G. C. Bazan, *Adv. Mater.* **2011**, *23*, 2367–2371. https://doi.org/https://doi.org/10.1002/adma.201004554.

[65] M. Li, A. H. Balawi, P. J. Leenaers, L. Ning, G. H. L. Heintges, T. Marszalek, W. Pisula, M. M. Wienk, S. C. J. Meskers, Y. Yi, F. Laquai, R. A. J. Janssen, *Nat. Commun.* **2019**, *10*, 2867. https://doi.org/10.1038/s41467-019-10519-z.

[66] T. Li, H. Zhang, B. Liu, T. Ma, J. Lin, L. Xie, D. Lu, *Macromolecules* **2020**, *53*, 4264–4273. https://doi.org/10.1021/acs.macromol.0c00579.

[67] S. Moro, N. Siemons, O. Drury, D. A. Warr, T. A. Moriarty, L. M. A. Perdigão, D. Pearce, M. Moser, R. K. Hallani, J. Parker, I. McCulloch, J. M. Frost, J. Nelson, G. Costantini, *ACS Nano* **2022**, *16*, 21303–21314. https://doi.org/10.1021/acsnano.2c09464.

[68] J. Hwang, D. B. Tanner, I. Schwendenaan, J. R. Reynolds, *Phys. Rev. B* **2003**, *67*, 115205.

[69] S. Nagamatsu, S. S. Pandey, *Sci. Rep.* **2020**, *10*, 20020. https://doi.org/10.1038/s41598-020-77022-0.

[70] E. C.-K. Wu, C. Z. Salamat, S. H. Tolbert, B. J. Schwartz, *ACS Appl. Mater. Interfaces* **2022**, *14*, 26988–27001. https://doi.org/10.1021/acsami.2c06449.

[71] P. Pingel, D. Neher, *Phys. Rev. B* **2013**, *87*, 115209. https://doi.org/10.1103/PhysRevB.87.115209.

[72] D. A. Stanfield, Y. Wu, S. H. Tolbert, B. J. Schwartz, *Chem. Mater.* **2021**, *33*, 2343–2356. https://doi.org/10.1021/acs.chemmater.0c04471.

[73] D. Scheunemann, E. Järsvall, J. Liu, D. Beretta, S. Fabiano, M. Caironi, M. Kemerink, C. Müller, *Chem. Phys. Rev.* **2022**, *3*, 21309. https://doi.org/10.1063/5.0080820.

[74] S. N. Patel, A. M. Glaudell, K.A. Peterson, E. M. Thomas, K. A. O'Hara, E. Lim, M. L. Chabinyc, *Sci. Adv.* **2023**, *3*, e1700434. https://doi.org/10.1126/sciadv.1700434.

[75] C. A. Palchucan, D. P. Lara, H. Correa, *Phys. A Stat. Mech. its Appl.* **2019**, *525*, 635–641. https://doi.org/https://doi.org/10.1016/j.physa.2019.03.052.

[76] A. Higgins, S. K. Mohapatra, S. Barlow, S. R. Marder, A. Kahn, *Appl. Phys. Lett.* **2015**, *106*, 163301. https://doi.org/10.1063/1.4918627.

[77] J. Euvrard, A. Revaux, P. -A. Bayle, M. Bardet, D. Vuillaume, A. Kahn, *Org. Electron.* **2018**, *53*, 135–140. https://doi.org/https://doi.org/10.1016/j.orgel.2017.11.020.

[78] J. Liu, G. Ye, H. G. O. Potgieser, M. Koopmans, S. Sami, M. I. Nugraha, D. R. Villalva, H. Sun, J. Dong, X. Yang, X. Qiu, C. Yao, G. Portale, S. Fabiano, T. D. Anthopoulos, D. Baran, R. W. A. Havenith, R. C. Chiechi, L. J. A. Koster, *Adv. Mater.* **2021**, *33*, 2006694. https://doi.org/https://doi.org/10.1002/adma.202006694.

[79] Y. Xuan, X. Liu, S. Desbief, P. Leclère, M. Fahlman, R. Lazzaroni, M. Berggren, J. Cornil, D. Emin, X. Crispin, *Phys. Rev. B* **2010**, *82*, 115454. https://doi.org/10.1103/PhysRevB.82.115454.

[80] H. Li, Z. Xu, J. Song, H. Chai, L. Wu, L. Chen, *Adv. Funct. Mater.* **2022**, *32*, 2110047. https://doi.org/https://doi.org/10.1002/adfm.202110047.

[81] J. Rivnay, S. Inal, B. A. Collins, M. Sessolo, E. Stavrinidou, X. Strakosas, C. Tassone, D. M. Delongchamp, G. G. Malliaras, *Nat. Commun.* **2016**, *7*, 11287. https://doi.org/10.1038/ncomms11287.

[82] W. B. Chang, H. Fang, J. Liu, C. M. Evans, B. Russ, B. C. Popere, S. N. Patel, M. L. Chabinyc, R. A. Segalman, *ACS Macro Lett.* **2016**, *5*, 455–459. https://doi.org/10.1021/acsmacrolett.6b00054.

[83] S. Mardi, D. Zhao, N. Kim, I. Petsagkourakis, K. Tybrandt, A. Reale, X. Crispin, *Adv. Electron. Mater.* **2021**, *7*, 2100506. https://doi.org/https://doi.org/10.1002/aelm.202100506.

[84] D. Venkateshvaran, M. Nikolka, A. Sadhanala, V. Lemaur, M. Zelazny, M. Kepa, M. Hurhangee, A. J. Kronemeijer, V. Pecunia, I. Nasrallah, I. Romanov, K. Broch, I. McCulloch, D. Emin, Y. Olivier, J. Cornil, D. Beljonne, H. Sirringhaus, *Nature* **2014**, *515*, 384–388. https://doi.org/10.1038/nature13854.

[85] S. P. Senanayak, A. Z. Ashar, C. Kanimozhi, S. Patil, K. S. Narayan, *Phys. Rev. B* **2015,** *91*, 115302. https://doi.org/10.1103/PhysRevB.91.115302.

[86] B. B. Patil, Y. Takeda, T. T. Do, A. Singh, T. Sekine, S. D. Yambem, S. Tokito, S. P. Singh, A. K. Pandey, P. Sonar, *Phys. status solidi* **2020**, *217*, 2000097. https://doi.org/https://doi.org/10.1002/pssa.202000097.

[87] J. Zessin, Z. Xu, N. Shin, M. Hambsch, S. C. B. Mannsfeld, *ACS Appl. Mater. Interfaces* **2019**, *11*, 2177–2188. https://doi.org/10.1021/acsami.8b12346.

[88] S. Takamaru, J. Hanna, H. Iino, *Jpn. J. Appl. Phys.* **2021**, *60*, SBBG08.

https://doi.org/10.35848/1347-4065/abeac3.

[89] H.-J. Jang, J. Wagner, H. Li, Q. Zhang, T. Mukhopadhyaya, H. E. Katz, *J. Am. Chem. Soc.* **2019**, *141*, 4861–4869. https://doi.org/10.1021/jacs.8b13026.

[90] A. E. Mansour, A. M. Valencia, D. Lungwitz, B. Wegner, N. Tanaka, Y. Shoji, T. Fukushima, A. Opitz, C. Cocchi, N. Koch, *Phys. Chem. Chem. Phys.* **2022**, *24*, 3109–3118. https://doi.org/10.1039/D1CP04985B.

[91] A. E. Mansour, D. Lungwitz, T. Schultz, M. Arvind, A. M. Valencia, C. Cocchi, A. Opitz, D. Neher, N. Koch, *J. Mater. Chem. C* **2020**, *8*, 2870–2879. https://doi.org/10.1039/C9TC06509A.

[92] S. Ma Andersen, *J. Fuel Cell Sci. Technol.* **2016**, *12*, 061010. https://doi.org/10.1115/1.4032430.